

**Seismic Noise Interferometry and Distributed Acoustic Sensing (DAS)  
Inverting for the Firn Layer S-Velocity Structure on Rutford Ice Stream, Antarctica**

Zhou, Wen; Butcher, Antony; Brisbourne, Alex M.; Kufner, Sofia Katerina; Kendall, J. Michael; Stork, Anna L.

**DOI**

[10.1029/2022JF006917](https://doi.org/10.1029/2022JF006917)

**Publication date**

2022

**Document Version**

Final published version

**Published in**

Journal of Geophysical Research: Earth Surface

**Citation (APA)**

Zhou, W., Butcher, A., Brisbourne, A. M., Kufner, S. K., Kendall, J. M., & Stork, A. L. (2022). Seismic Noise Interferometry and Distributed Acoustic Sensing (DAS): Inverting for the Firn Layer S-Velocity Structure on Rutford Ice Stream, Antarctica. *Journal of Geophysical Research: Earth Surface*, 127(12), Article e2022JF006917. <https://doi.org/10.1029/2022JF006917>

**Important note**

To cite this publication, please use the final published version (if applicable).  
Please check the document version above.

**Copyright**

Other than for strictly personal use, it is not permitted to download, forward or distribute the text or part of it, without the consent of the author(s) and/or copyright holder(s), unless the work is under an open content license such as Creative Commons.

**Takedown policy**

Please contact us and provide details if you believe this document breaches copyrights.  
We will remove access to the work immediately and investigate your claim.

## Seismic Noise Interferometry and Distributed Acoustic Sensing (DAS): Inverting for the Firn Layer *S*-Velocity Structure on Rutford Ice Stream, Antarctica

Wen Zhou<sup>1,2</sup> , Antony Butcher<sup>1</sup> , Alex M. Brisbourne<sup>3</sup> , Sofia-Katerina Kufner<sup>3,4</sup> , J-Michael Kendall<sup>5</sup> , and Anna L. Stork<sup>6</sup> 

<sup>1</sup>School of Earth Sciences, University of Bristol, Bristol, UK, <sup>2</sup>Now at Department of Geoscience and Engineering, Delft University of Technology, Delft, The Netherlands, <sup>3</sup>British Antarctic Survey, Cambridge, UK, <sup>4</sup>Karlsruhe Institute of Technology, Geophysical Institute, Karlsruhe, Germany, <sup>5</sup>Department of Earth Sciences, University of Oxford, Oxford, UK, <sup>6</sup>Silixa Ltd, Elstree, UK

**Key Points:**

- Distributed acoustic sensing (DAS) is used for the first time to derive the *S*-wave velocity structure and anisotropy of the firn layer in Antarctica
- DAS seismic interferograms are greatly improved through selective stacking and cross-correlation with a geophone
- Our method is suitable for large-scale measurements and is feasible in the presence of ice lenses where refraction methods are inadequate

**Supporting Information:**

Supporting Information may be found in the online version of this article.

**Correspondence to:**

W. Zhou,  
wz18709@bristol.ac.uk

**Citation:**

Zhou, W., Butcher, A., Brisbourne, A. M., Kufner, S.-K., Kendall, J.-M., & Stork, A. L. (2022). Seismic noise interferometry and distributed acoustic sensing (DAS): Inverting for the firn layer *S*-velocity structure on Rutford Ice Stream, Antarctica. *Journal of Geophysical Research: Earth Surface*, 127, e2022JF006917. <https://doi.org/10.1029/2022JF006917>

Received 13 SEP 2022

Accepted 9 DEC 2022

**Author Contributions:**

**Conceptualization:** Wen Zhou, Antony Butcher, J-Michael Kendall, Anna L. Stork

**Data curation:** Alex M. Brisbourne, Sofia-Katerina Kufner, J-Michael Kendall

**Formal analysis:** Wen Zhou, Antony Butcher, Alex M. Brisbourne

**Funding acquisition:** Alex M. Brisbourne, J-Michael Kendall, Anna L. Stork

**Methodology:** Wen Zhou

© 2022. The Authors.

This is an open access article under the terms of the [Creative Commons Attribution License](https://creativecommons.org/licenses/by/4.0/), which permits use, distribution and reproduction in any medium, provided the original work is properly cited.

**Abstract** Firn densification profiles are an important parameter for ice-sheet mass balance and palaeoclimate studies. One conventional method of investigating firn profiles is using seismic refraction surveys, but these are difficult to upscale to large-area measurements. Distributed acoustic sensing (DAS) presents an opportunity for large-scale seismic measurements of firn with dense spatial sampling and easy deployment, especially when seismic noise is used. We study the feasibility of seismic noise interferometry (SI) on DAS data for characterizing the firn layer at the Rutford Ice Stream, West Antarctica. Dominant seismic energy appears to come from anthropogenic noise and shear-margin crevasses. The DAS cross-correlation interferometry yields noisy Rayleigh wave signals. To overcome this, we present two strategies for cross-correlations: (a) hybrid instruments—correlating a geophone with DAS, and (b) stacking of selected cross-correlation panels picked in the tau-p domain. These approaches are validated with results derived from an active survey. Using the retrieved Rayleigh wave dispersion curve, we inverted for a high-resolution 1D *S*-wave velocity profile down to a depth of 100 m. The profile shows a “kink” (velocity gradient inflection) at ~12 m depth, resulting from a change of compaction mechanism. A triangular DAS array is used to investigate directional variation in velocity, which shows no evident variations thus suggesting a lack of azimuthal anisotropy in the firn. Our results demonstrate the potential of using DAS and SI to image the near-surface and present a new approach to derive *S*-velocity profiles from surface wave inversion in firn studies.

**Plain Language Summary** The density distribution (density change with depth) over tens of meters at the top of a glacier is an important feature of ice-sheet mass balance and palaeoclimate research. It can be estimated using the empirical relationship between density and seismic *P*-wave velocity. The *P*-wave velocity can be measured using a seismic refraction survey with geophones and active sources. However, refraction seismic surveys are expensive for measurements over large areas. Distributed Acoustic Sensing (DAS) using fiber optic cables to detect seismic waves is an emerging dense spatial sampling seismic acquisition technology. It can be used in conjunction with seismic noise cross-correlation to make large-scale measurements easier and cheaper than with conventional geophones. We investigate the feasibility of this approach on Rutford Ice Stream, West Antarctica, and propose two approaches to improve DAS seismic-noise cross-correlation results. Surface waves are retrieved by seismic noise cross-correlation and are used to estimate the *S*-wave velocity structure. Our *S*-velocity profile resembles an independently measured *P*-velocity in-shape and presents a velocity gradient inflection—related to changes in the snow compaction mechanism. We show that DAS and seismic noise interferometry can be used for future firn measurements, but also more generally in studies of the near-surface.

### 1. Introduction

Firn is partially compacted granular snow, the intermediate stage between fresh snow and the underlying glacial ice. It has a depth-increasing density which results from the densification and metamorphosis of snow into glacial ice. Through burial by subsequent accumulation, the overburdened weight compacts the snow and reduces porosity by grain packing, deformation, and sintering (Alley, 1987; Cuffey & Paterson, 2010). The depth-density profile is controlled primarily by the temperature and snow accumulation rate and is highly variable due to the

**Project Administration:** Antony Butcher  
**Software:** Wen Zhou, Antony Butcher  
**Writing – original draft:** Wen Zhou  
**Writing – review & editing:** Wen Zhou,  
Antony Butcher, Alex M. Brisbourne,  
Sofia-Katerina Kufner, J-Michael  
Kendall, Anna L. Stork

broad range of climatic conditions across the Antarctic continent (e.g., van den Broeke, 2008). Knowledge of the firn layer is crucial for improving altimetric mass-balance estimates (Shepherd et al., 2012) and palaeoclimate reconstructions (Craig et al., 1988). Additionally, studying the firn layer properties may help to constrain models of surface melt leading to ice shelf retreat (van den Broeke, 2005). However, other effects such as shear deformation along ice stream shear-margin (Riverman et al., 2019), and glacier dynamics (Hollmann et al., 2021) also influence firn structure, which suggests a comprehensive study of the Antarctica firn may be required to improve ice-sheet mass balance estimates.

Conventionally, the structure and densification profile of firn is directly measured from ice core or borehole logging (e.g., Morris et al., 2017), or indirectly using for example, seismic *P*-wave refraction (e.g., Kirchner & Bentley, 1979) or radar measurements (e.g., Case & Kingslake, 2022). A specific version of seismic refraction inversion was developed for the investigation of firn structures by Kirchner and Bentley (1979). The method uses curve fitting with a double-exponential form applied to diving wave travel times, prior to a Wiechert-Herglotz-Bateman (WHB) velocity-depth inversion (Slichter, 1932). These results are commonly used to correct seismic reflection surveys for near-surface effects (e.g., Peters et al., 2006; Smith, 1997), derive elastic properties of firn (King & Jarvis, 2007; Schlegel et al., 2019), and investigate its spatial variations and azimuthal anisotropy.

The presence of anisotropy in the firn layer has been reported previously. Kirchner and Bentley (1990) indicate substantial azimuthal anisotropy in the upper 30–40 m and state that simple transverse isotropy with a vertical symmetry axis (VTI) expected from firn compaction is not always appropriate. A recent study by Hollman et al. (2021) infers seismic anisotropy in the firn on the Amery Ice Shelf in the proximity of former shear margins. Polarimetric radar measurements have also indicated the presence of complex near-surface anisotropy on both Whillans and Rutford Ice Streams (Jordan et al., 2020, 2022), in general related to ice flow and surface strain rates.

Although the WHB method is viable for both *P*- and *S*-wave velocity measurement, the former is by far the most widely used due to the greater ease of generation and identification of *P*-wave energy. However, King and Jarvis (2007) observed a variation of the Poisson ratio with depth in the firn layer, suggesting that measuring *S*-wave velocity is important for studying firn elasticity and densification.

In addition, because a commonly used WHB refraction inversion method fits a double exponential velocity profile to the travel-time data, it can only apply to a typical compacted firn with monotonically increasing seismic velocity over depth and with one “kink” (critical density) from a change of compaction mechanism and without any ice lenses (Kirchner & Bentley, 1979).

Furthermore, with conventional geophone sensors, it is time-consuming and more expensive to apply the refraction survey to cover a large area, because of the dense receiver spacing at the near offset required by the WHB inversion. Thus, most previous refraction surveys are limited to a scale of a few hundred meters (Hollmann et al., 2021; King & Jarvis, 2007; Schlegel et al., 2019), effectively, point measurements compared with the large area of Antarctica. Recently, Riverman et al. (2019) conducted a 40 km refraction survey but with a sparse geophone spacing of 20 m which showed a poor resolution in the upper ~20 m of the firn.

Therefore, any new seismic technique capable of measuring *S*-wave velocities, measuring firn layer anomalies including ice lenses or low-velocity zones, or with better scaling capabilities, would be beneficial for future studies of firn. In this study, we investigate the feasibility of using DAS data, seismic noise interferometry (SI), and surface (Rayleigh) wave inversion to address the aforementioned problems by performing distributed acoustic sensing (DAS) measurements on Rutford Ice Stream, West Antarctica.

In recent years, there has been a rapid development of DAS in seismic acquisition. DAS is an optical fiber sensing technology that offers the potential of broadband frequency recording and near-continuous spatial sampling of earth strain and temperature variation signals (Ajo-Franklin et al., 2019; Ide et al., 2021). Its unprecedented spatial sampling could improve the spatial resolution of subsurface seismic images (Ajo-Franklin et al., 2019; Dou et al., 2017; Lellouch et al., 2019; Rodríguez Tribaldos & Ajo-Franklin, 2021; Rodríguez Tribaldos et al., 2021; Spica, Nishida, et al., 2020; Williams et al., 2019). The sensing element of DAS is the optical fiber without electronic or mechanical components, which makes the technology an attractive option for long-term, low-maintenance deployments for glacial studies (Booth et al., 2020; Brisbourne et al., 2021; Hudson et al., 2021; Walter et al., 2020), for in-situ measurement in deep boreholes for an active fault (Lellouch et al., 2019), geothermal, hydrocarbon storage (Correa et al., 2018; Mateeva et al., 2017) or hydrogen storage monitoring, and for

submarine environments (Lior, Sladen, et al., 2021; Spica, Nishida, et al., 2020; Williams et al., 2019). It could also be suitable for critical infrastructure (e.g., nuclear plants; Butcher et al. (2021), dams, embankments, etc.).

Seismic noise interferometry is a simple and convenient method, from both data processing and acquisition perspectives. Many studies have used the method to retrieve surface waves for studying ice-sheets. For example, using broadband seismometers, Walter et al. (2015) used surface wave energy from crevasse events to derive the Rayleigh wave response between stations. Sergeant et al. (2020) retrieved Rayleigh waves between stations at a number of sites in Greenland and the Alps using a range of noise sources. Also in the Alps, at Glacier de la Plaine Morte, Switzerland, measurements of azimuthal variation in Rayleigh wave velocity indicate that crevasses cause up to 8% anisotropy (Lindner et al., 2019). Chaput et al. (2022) investigated noise interferometry and H/V for characterizing the firn layer in West Antarctica. DAS has recently been used in glacier settings for noise interferometry by Walter et al. (2020), who retrieved Rayleigh wave (above 10 Hz) from cross-correlations.

Using data acquired with conventional geophones or seismometers, surface wave inversion has been used previously to study firn structures. For instance, Picotti et al. (2015) used surface waves acquired from a refraction survey to invert for the  $S$  velocity profile, at Whillans Ice Stream; Diez et al. (2016) retrieved Rayleigh and Love waves from anthropogenic noise and inverted them for  $S$  velocity (SH and SV) profiles at the Ross Ice Shelf; Chaput et al. (2022) also used anthropogenic seismic noise to retrieve Rayleigh waves and inverted for  $S$  velocity at central west Antarctica. Compared with conventional seismometers or geophones, DAS has higher instrument self-noise (e.g., optical system noise) which can obscure the weak seismic “noise” that is the crucial “signal” for noise interferometry. Nevertheless, in recent years, there have been successful applications of DAS for ambient surface wave imaging in submarine environments, using microseism noise at 0.6–1 Hz (Spica, Nishida, et al., 2020), 0.5–5 Hz (Cheng et al., 2021) and 1–3 Hz (Lior, Mercerat, et al., 2022). The advantage of recording in the offshore environment is the stable seafloor temperature and shorter distance to microseism noise sources. Onshore applications have been also successful (e.g., Dou et al., 2017; Rodríguez Tribaldos & Ajo-Franklin, 2021; Spica, Pertou, et al., 2020), with reported applications mostly limited to urban environments with strong anthropogenic (traffic, mechanical) noise at frequencies typically above 5 Hz. However, it is still rare to apply DAS noise interferometry in remote non-urban areas onshore, especially in low ambient noise environments, such as the Antarctic Ice Sheet.

In this manuscript, first, we present the field experiment and data acquisition at the Rutford Ice Stream in West Antarctica. Second, we demonstrate that Rayleigh waves can be retrieved through noise interferometry using data acquired on a linear-configured DAS cable. The interferograms can be improved with hybrid-instrumenting and selective stacking of noise cross-correlations. Third, the fundamental mode Rayleigh wave dispersion curve is extracted and inverted to obtain an  $S$ -wave velocity ( $V_s$ ) profile. We verify the method by comparison with dispersion analysis of the surface waves captured by an active survey using a sledgehammer and plate source. Finally, we use the data from a triangular-configured DAS array to investigate the seismic anisotropy of the firn.

## 2. Field Experiment and Data Acquisition

Rutford Ice Stream (Figure 1a) is a fast-flowing ice stream draining part of the West Antarctic Ice Sheet into the Ronne Ice Shelf. At the experiment location, 40 km upstream of the grounding line, it is around 25 km wide and 2,200 m thick, with an ice flow of  $\sim 380 \text{ m a}^{-1}$  (Murray et al., 2007).

Between 11 and 24 January 2020, an experiment was carried out at Rutford Ice Stream (Figure 1a) utilizing both DAS and geophones for passive and active surveys. The seismic arrays were collocated and installed at the center of the ice stream where the surface is mostly flat (Figure 1a), to record the regularly occurring icequakes originating from the base of the glacier where it slides over the bed (Hudson et al., 2021; Kufner et al., 2021; Smith et al., 2015). A second aim was to image the firn layer using seismic noise and active sources. The DAS data were acquired using a Silixa iDAS v2 interrogator connected to a 1 km six channel tight buffered single mode fiber optic cable. The cable was deployed in linear and triangular configurations, successively. The interrogator measures strain rates along the optical fiber every 1 m, with a gauge length of 10 m. For the passive measurement, we used a 1 kHz sampling rate. A petrol generator (Honda EU10i 1 kW) was deployed as the power supply, which was located on the snow surface, 50 m from the interrogator in a direction aligned with the orientation of the fiber (Figure 1b).

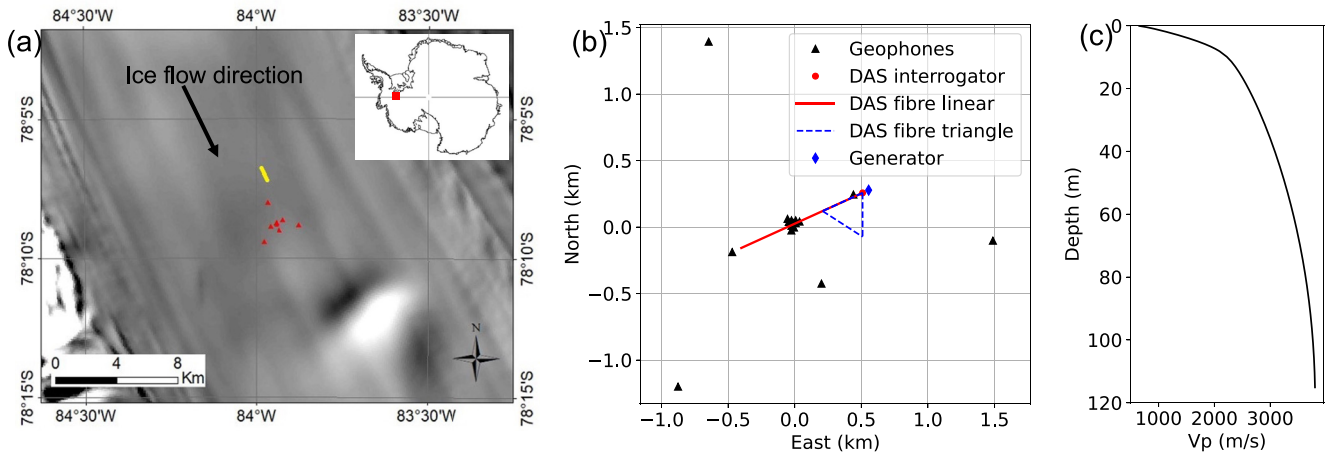


**Figure 1.** (a) Location of the seismic experiment on Rutford Ice Stream. The background is Moderate-resolution Imaging Spectroradiometer imagery (Scambos et al., 2007). Geophones are shown as red dots. The yellow line indicates the location of a previous refraction survey (Smith et al., 2021). (b) The relative position (reference at the center of the geophone array) of instruments. Geophones (black triangles) were designed for array processing. Distributed acoustic sensing (DAS) fibers (red solid line and blue dashed line) were connected to the DAS interrogator at the east end. The generator (diamond) sits 50 m away from the interrogator. (c) Firn  $P$ -wave velocity profile from a refraction experiment (Smith et al., 2021), using an expanding interval of vertical component geophones.

The cable was laid in the track of a snowmobile and initially deployed without burial, but subsequently buried with a layer of approximately 5 cm of snow. Hudson et al. (2021) described these data and investigated the suitability of DAS for micro-seismicity (icequakes) monitoring. Butcher et al. (2021) further explored the utility of DAS data using array-based processing methods. Hudson et al. (2021) also investigated the difference between buried and unburied cables. They showed that even shallow burial of the cable made a significant difference in attenuating the unwanted noise and enhancing the lower frequency (below 1 Hz) signal. For frequencies 1–70 Hz, the buried cable has a lower noise level due to improved coupling and reduced wind noise. Since only the seismic noise is useful for imaging the subsurface, we concentrate on the period when the cable was buried.

The geophone network consisted of sixteen 4.5 Hz 3-component Geospace GS-11D geophones with Reftek RT130 dataloggers with a 1 kHz sample rate. The geophone array layout was primarily designed to detect and locate icequakes (Figure 1b). Three geophones were collocated in-line with the fiber, and approximately in the middle and at either end of the linear DAS array.

In addition to the passive measurements, an active seismic survey was also acquired along the linear array using a sledgehammer (4.5 kg) and plate source. These signals were recorded by the interrogator at an 8 kHz sampling rate. At the 21 source locations (every 50 m from 10 to 1,000 m along the fiber) either two or four hammer blows were acquired. In general, the data quality of these shot-gathers is high, with signals captured across the entire 1 km linear array without the need for stacking. An example shot-gather from this survey is presented in Figure 2, which shows dominant seismic phases including refracted (diving)  $P$ -waves and Rayleigh waves, as indicated. The shot times are constrained from the onset of the DAS record (Figure 2b, the first record is the strain generated by the hammer plate impact). Due to the averaging effect of the 10 m gauge length, very near offset DAS recordings are distorted (Figure 2b) which limits the accuracy of the near-surface  $V_p$  in a WHB refraction inversion (Williams, 2022).

A conventional  $P$ -wave seismic refraction survey was previously acquired 2.6 km upstream of the study area (Figure 1a), using a surface source and expanding spread of vertical component geophones out to a maximum offset of 980 m, as part of the site survey for the BEAMISH subglacial drilling project (Smith et al., 2021). Using this refraction data set, we derived a  $P$ -wave velocity-depth profile using the WHB based inversion method of Kirchner and Bentley (1979) (Figure 1c). With this method, Kirchner and Bentley (1990) report velocity uncertainty of  $\pm 60$  m/s near the surface, reducing to  $\pm 15$  m/s at 50 m depth on the Ross Ice Shelf, which we assume is similar in our inversion given the similarity of firn structures of the two sites.

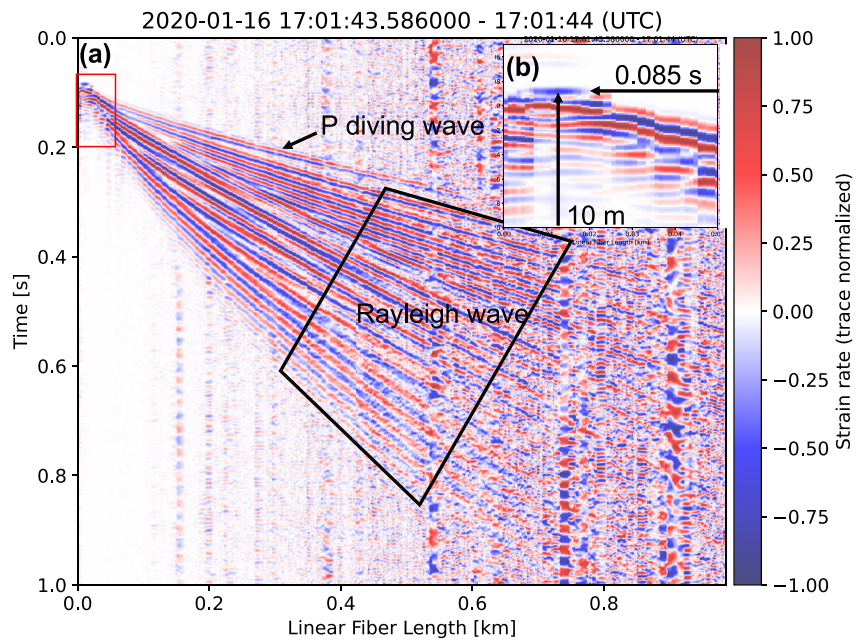


**Figure 2.** An example of active shot data from a hammer and plate source. (a) A shot gather on the 1 km linear fiber (1 m channel distance plotted), with the source at 10 m from one end of the fiber. The strain rate waveforms are normalized over each Distributed acoustic sensing (DAS) channel. Signal is bandpass filtered 5–100 Hz. Time 0 s is not the trigger time, but an arbitrary stamp as shown in the figure. (b) is a zoom-in of the (a) as indicated by the red box. Around the shot location (10 m), the first arrivals are flat, which is an artifact of the 10 m DAS gauge length.

### 3. Seismic Noise Interferometry

#### 3.1. Cross-Correlation Interferometry

Since the work of Shapiro et al. (2005) and Shapiro and Campillo (2004), SI has become a well-established technique to probe subsurface seismic properties, especially with surface waves derived from ambient microseismic noise (Bensen et al., 2007; Shapiro & Campillo, 2004; Shapiro et al., 2005). It is termed SI as the method utilizes continuous seismic records without specifying their sources (location and origin time) and assuming it is random and distributed isotropically in an azimuthal sense. An extensive literature review of the subject is provided by Snieder & Larose (2013). In this paper, we term the records as “signals,” especially when we investigate their characters. But when applying seismic interferometry, coherent seismic signals and noise are collectively referred to as “seismic noise” and we do not distinguish between them.

Recent studies have implemented SI with DAS data in a borehole (Lellouch et al., 2019), submarine (Cheng et al., 2021; Spica, Perton, et al., 2020), and urban environment (Ajo-Franklin et al., 2019; Dou et al., 2017; Spica, Perton, et al., 2020). Most of those studies calculate interferograms by cross-correlating (CC) one DAS channel, termed the “virtual source” with all channels within the array and then apply stacking to enhance coherent signals. This approach is adopted from the processing workflow for processing conventional seismometers or geophones data, and we describe this in a detailed processing flow in Figure S6 in Supporting Information S1.

Prior to the interferometry analysis, we seek to characterize the DAS seismic recordings (nature of the noise and noise sources). For a conventional seismic array, seismic noise is analyzed with beamforming, which estimates the apparent velocity and azimuth of the coherent wavefield, such as in Chaput et al. (2022). van den Ende & Ampuero (2021) applied beamforming to DAS recorded earthquake signal using a fiber with a 2D deployment. However, with our 1D linear array, it is not feasible to perform the beamforming analysis to determine noise azimuth. We thus manually inspect the DAS data in the time-space (time dimension on one axis and channel distance on the other) plot for three frequency bands (<1, 1–10, and 10–100 Hz). Examples of seismic noise and signals are presented in Supporting Information S1. First, at higher frequencies (10–100 Hz), we show that seismic noise is generated by a snowmobile (Figure S1 in Supporting Information S1) which is mostly used around the interrogator. Note basal icequakes at frequencies 30–150 Hz are also recorded as reported by Hudson

et al. (2021). At intermediate frequencies (1–10 Hz), the seismic signals are dominated by surface wave events (Figure S2 in Supporting Information S1). Using the geophone array, we locate those surface wave events, and find most of them occur close to the shear margin of the ice stream (Figure S5 in Supporting Information S1), thus we suspect they are crevasse events. Similar crevasse signals have contributed to ambient noise analysis at an alpine glacier (Walter et al., 2015, 2020). Lastly, we show that low-frequency DAS signals (below 1 Hz) have extremely low propagation velocities of a few m/s and the amplitudes are correlated with wind speed (Figure S3 in Supporting Information S1).

To apply the SI analysis, first we slice the continuous data into small segments in the time-domain and then calculate the spectrally whitened CCs:

$$c_i(\omega) = \frac{1}{N} \sum_{n=1}^N \frac{r_i(\omega)s(\omega)^*}{\sqrt{r_i(\omega)^2 s(\omega)^2}}, \quad i = 1, 2, \dots, m$$

For each segment  $n$ , we decimate the sampling rate to 200 Hz and then apply a cosine taper. A Fourier transform is applied for each channel so the virtual source channel and each receiver channel are represented in the frequency-domain:  $s(\omega)$ ,  $r_i(\omega)$  ( $m = 1,000$  for the linear DAS array). Since the desired seismic noise is above 1 Hz, we choose a segment length of 10 s, with an overlap of 5 s. To keep the process simple, we do not apply time-domain normalization (1-bit) or remove the basal icequakes signals before CCs. The power spectra,  $r_i(\omega)^2$  and  $s(\omega)^2$ , are smoothed by a 21-sample moving average, a process known as spectral whitening. The cross-correlations over each segment  $c_i(\omega)$  are stacked over every 2 min. These 2-min CCs are stored for further processing.

Although the “CC-stacking” workflow is applied here, we note that to directly retrieve surface wave dispersion data we could stack data in the frequency-wavenumber ( $f$ - $k$ ) domain, without calculating the CC (e.g., Cheng et al., 2019; Park et al., 2004; Spica, Nishida, et al., 2020). However, after  $f$ - $k$  domain stacking, phase information is lost, and the data cannot be converted back to the time domain for inspection or further analysis.

### 3.2. Choice of Virtual Source: DAS Versus Geophone

DAS interferogram profiles are obtained through linearly stacking 2-min CC panels over the entire recording period of 5 days (Figures 3a and 3b). We produce two different interferograms. The first uses the DAS channel at 600 m as a virtual source (Figure 3a), while the second takes the vertical component of a co-located geophone, positioned  $\sim 570$  m along the fiber, as the virtual source (Figure 3b). The CCs calculated with a DAS virtual source (Figure 3a) have the highest amplitude at 0 s delay time, which is due to coherent DAS instrument noise which occurs instantaneously across the array (often referred to as “common mode” noise, Figure S4e in Supporting Information S1), whilst the seismic response, especially at a lower frequency and larger distance, are faint.

In the second approach (Figure 3b), a geophone is used as the virtual source to cross-correlate with DAS channels, which we term hybrid instrumenting CC. A clearer CC profile is retrieved, and the 0 s delay time instrument noise is eradicated. The seismic signals become clear, and we can see that they are traveling both forward (from 0 m to 1 km along the cable) and backward with an apparent velocity of  $\sim 1.7$  km/s. Its dispersive nature shows that it is a surface wave. Since DAS records longitudinal strain along the fiber, parallel to the propagation direction of the retrieved signal, this surface wave is classified as a Rayleigh wave. The coherent response between the vertical component geophone and the horizontal component DAS is the result of Rayleigh wave elliptical particle motion in the vertical plane, parallel to the direction of propagation. We have tested the process with the horizontal component (East component, near parallel to the DAS cable) of the geophone, which showed little difference in terms of signal quality.

Figure 3b shows features such as a high frequency (33.3 Hz) oscillating noise that decays away from the start of the line at 0 m. This strong harmonic signal is generated by the petrol generator (Figure S1c in Supporting Information S1). There is also strong 9 Hz oscillation noise around 560 and 570 m, which is likely strain produced by the wind-driven movement of two marker-flags (used to indicate the location of the geophones). Since this 9 Hz noise is very localized, it does not influence further analyses.

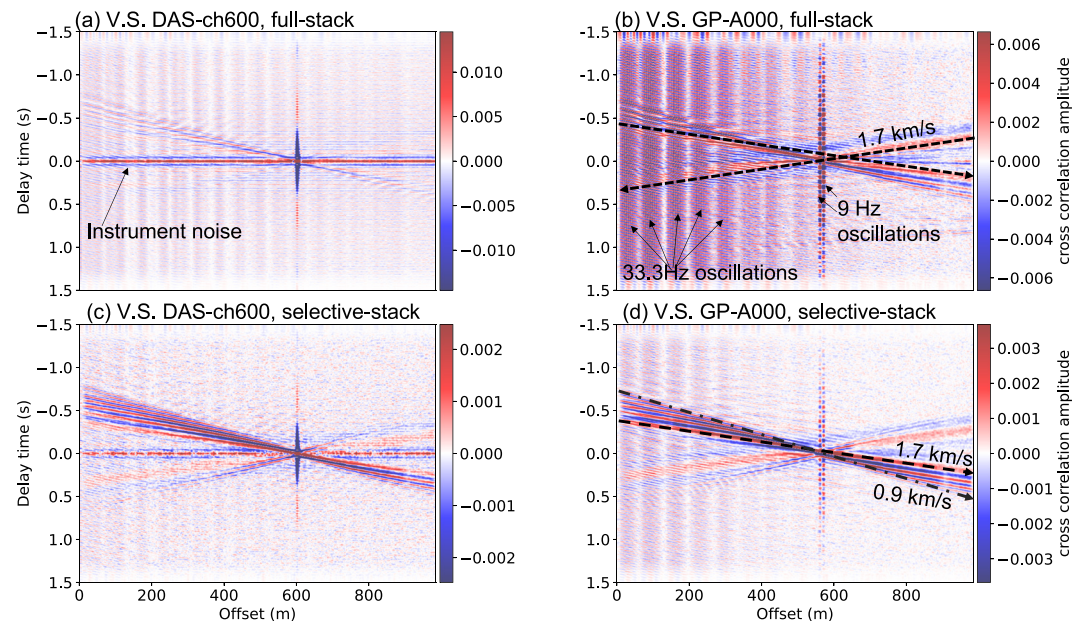


**Figure 3.** Cross-correlations (CCs) (1–30 Hz, second order Butterworth bandpass zero-phase filtered) from 4 approaches. (a) Stacked cross-correlations, a virtual shot gather, with a virtual source at Distributed Acoustic Sensing channel at 600 m. (b) Same as (a) but with a virtual source at a geophone (A000) located close to channel 570 m. (c) Selective-stacked CCs for the same data as (a). (d) Selective-stacked CCs for the same data as (b). Note for each panel, the color scale is saturated at the median over maximal values from each channel for visualization.

### 3.3. Selective Stacking of Cross-Correlations

To improve the quality of the final interferogram image, previous studies have introduced more sophisticated techniques of stacking CCs, such as phase-weighted stacking (Schimmel & Paulssen, 1997; Schimmel et al., 2011) and SNR-weighted stacking (Cheng et al., 2015). The phase-weighted stacking suppresses incoherent noise between two CCs and has several advantages over a standard linear stack (Dou et al., 2017). This approach, however, assumes that coherent seismic noise is continuous over each time span of CCs. In our case, most of the seismic signal recorded in our data set are transient in nature; an exception is the harmonic signal from the generator. SNR-weighted stacking is based on the SNR of CCs and has been shown to perform well for anthropogenic seismic noise above 2 Hz, which are often transient and spatially variable (Cheng et al., 2015). Manual inspection of our 2-min CCs shows that some retrieved Rayleigh wave signals have very low SNR on individual channels. Such CCs would be down-weighted if applying SNR-weighted method. However, these weak Rayleigh wave signals are visible because of their spatial coherency, which inspired us to use spatial coherency to detect and select data containing Rayleigh wave signals.

The studies on anthropogenic noise interferometry by Zhou and Paulssen (2020) introduced a pre-processing step by detecting and extracting noise, such as trains, for stable time-lapse CCs. That approach, however, requires a sophisticated detection scheme. Cheng et al. (2019) applied tau-p transform on processed time domain data and selected segments based on an SNR defined from the distribution of slowness ( $p$ ).

Rather than selecting from the raw data, a CC-based selection scheme is computationally cheaper. Previous noise interferometry studies have selected CCs before stacking based on SNR (Olivier et al., 2015), amplitude decay (Dou et al., 2017), and apparent velocity from 2D array beamforming analysis (Vidal et al., 2014). We term these CC selection schemes as selective stacking.

For the linear-configured DAS array, applying the linear tau-p transform (slant-stack) (Diebold & Stoffa, 1981) could highlight spatially coherent signals which have a near straight-line moveout. We thus applied the tau-p transform to each 2-min CCs panel for the frequency band 3–25 Hz. Following a manual inspection of the tau-p diagrams (two examples are shown in Figure 4), we find the tau-p domain maximal amplitude is a sufficient and easy selection criterion. For CCs between geophone and DAS, we set the criteria as follows: (a) maximal amplitude



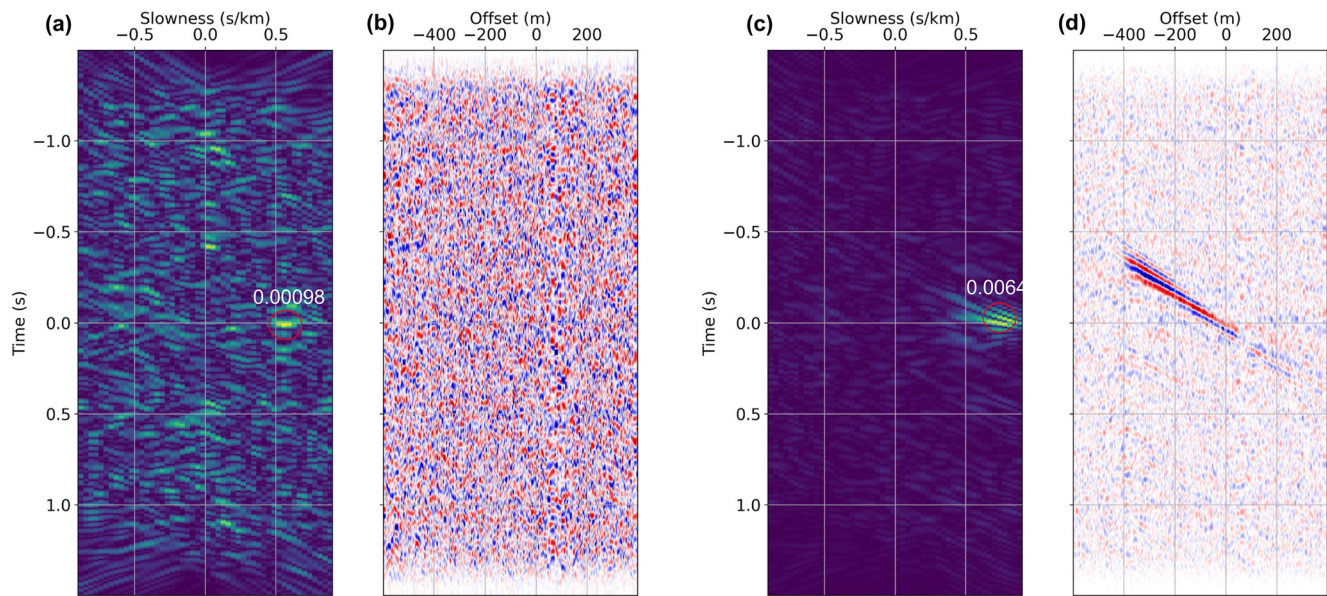


**Figure 4.** Examples of tau-p transform of cross-correlations (CCs) (a, b) Example of a noisy CC panel, with peak amplitude in the tau-p domain 0.00098 (c, d) Example of a selected CC panel, with tau-p domain peak amplitude 0.0064.

no lower than 0.0014 (CC coefficient), (b) maximum locates at delay time close to zero ( $0 \pm 0.05$  s), and with an apparent velocity smaller than 2,500 m/s (slowness  $< -0.4$  or  $> 0.4$  s/km).

These two criteria allow the selection of CCs containing clear surface wave signals. The example in Figure 4a shows a slowness larger than 0.4 s/km and delay time close to zero, but the maximal amplitude (0.00098) is much smaller than 0.0014, therefore this CC panel is rejected. The strong signal shown in Figure 4c meets the criteria and is therefore selected.

Of the 3,068 2-min CC panels (5 days with a few hours of data loss), 453 met the selection criteria and were linearly stacked. The selectively stacked CCs (Figures 3c and 3d) show much higher SNR of the seismic response compared to those for the non-selective (Figures 3a and 3b). Although for a DAS virtual source (Figure 3c), the coherent instrument noise is still present in the selectively stacked CCs, the seismic response is clearer since a large component of instrument noise is removed.

We achieve the best quality CCs for this data set by combining a geophone as virtual source with selective stacking (Figure 3d). The signal shows clear dispersion as the higher frequency content has a steeper slope, which indicates a lower velocity.

## 4. Dispersion and 1D Velocity Structure

### 4.1. Dispersion Analysis

Surface wave phase velocity dispersion curves can be extracted in the frequency-velocity ( $f$ - $v$ ) domain. This can be achieved using a frequency-wavenumber ( $f$ - $k$ ) transform, or through a sweeping slant stack or tau-p transform for narrowly band-passed multichannel data (Xia et al., 2007). Such an approach is often termed multichannel analysis of surface waves (MASW) (Park et al., 1999; Xia et al., 1999), or PMASW for passively retrieved surface waves from CC (Cheng et al., 2016). In this study, a 2D Fourier transform ( $f$ - $k$  transform) is applied after tapering the CCs with a Hann window in both the time and space dimensions. We further stack the positive and negative parts of the wavenumber domain to enhance the signal. These  $f$ - $k$  diagrams (Figure S7 in Supporting Information S1) are then converted to the frequency-phase velocity ( $f$ - $v$ ) domain (e.g., Figure 5a). Multiple modes of Rayleigh waves are present in both datasets, but for simplicity, only the fundamental mode dispersion curve is extracted by picking the local maximal amplitude.

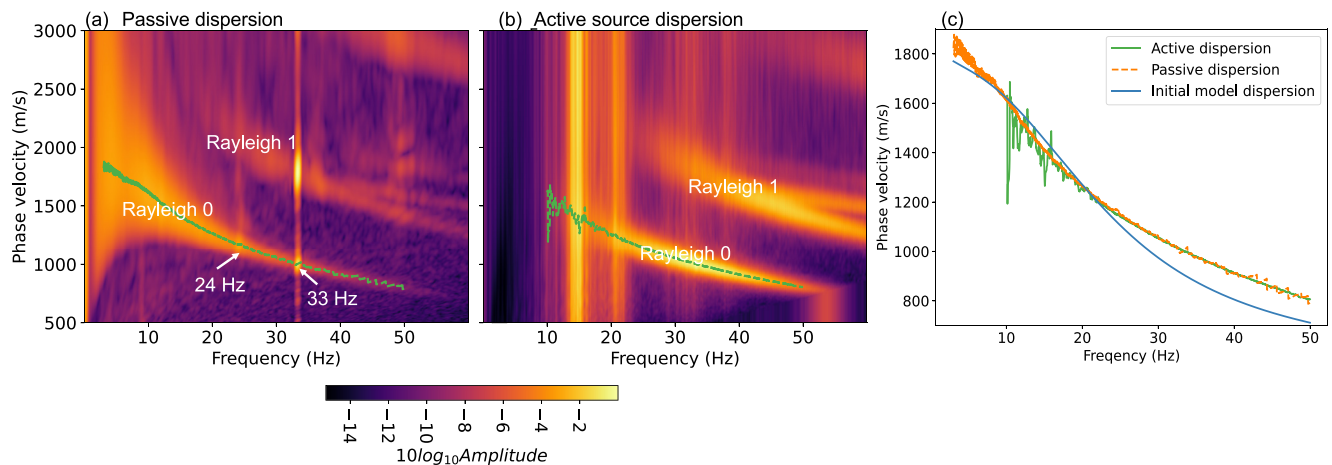


**Figure 5.** Extracting Rayleigh wave fundamental mode (Rayleigh 0, green dashed lines) dispersion curve from the frequency-velocity domain, by picking the local maximum amplitude. (a) Frequency-velocity plot of the stacked Cross-correlations (CCs). The Rayleigh 0 mode dispersion curve is extracted from 3 to 50 Hz. Note, that *two oscillatory signals* are present at 24 and 33 Hz. (b) Stacked frequency-velocity plot of the 21 active shots. The Rayleigh 0 mode is extracted from 10 to 50 Hz. (c) Comparing observed (CCs and active shots) with initial model dispersion curves, from 3 to 50 Hz. The initial  $V_s$  model is presented in Figure 6.

For comparison, we also analyzed an active source seismic data set. Data were collected from 21 shot locations (2 or 4 shots for every 50 m) using a sledgehammer source. This survey is processed to produce a frequency-velocity plot, which is similar to that obtained from the CCs. For each shot gather, DAS channels are split into two sides by the location of the active source. The  $f$ - $k$  transform is separately applied to each side to avoid interference. Then, the data are stacked in the  $f$ - $k$  domain: (a) for each  $f$ - $k$  diagram, the negative and the positive wavenumbers are stacked; (b) for each shot gather, the two  $f$ - $k$  diagrams are stacked; (c) for all shot gathers, they are further stacked to produce a single  $f$ - $k$  diagram. Lastly, the  $f$ - $k$  diagram is converted to the  $f$ - $v$  domain (Figure 5b).

The fundamental mode (Rayleigh 0) and the first higher mode (Rayleigh 1) from both the passive CCs and the active sources are shown in Figure 5. In general, there is strong agreement between the two approaches in the frequency range of 15–50 Hz. Figure 5c shows the extracted Rayleigh 0 dispersion curves, showing a good agreement between the two approaches. This provides us with confidence that the methods adopted when producing the noise interferograms are appropriate. The passive data set contains relatively lower frequency signals, and its dispersion curve is well constrained down to 3 Hz (Figure 5a). From Figure 5b, we see that the stacked active shots data contain signals mostly above 10 Hz with dispersion most stable between 15 and 50 Hz. This is likely due to the lack of low-frequency energy generated by the hammer and plate source. At around 33.3 Hz, there is a small but sharp reversal of velocity from the CCs derived dispersion (Figure 5a), which is due to the strong generator noise observed at 33.3 Hz (Figure 3 and Figure S1d in Supporting Information S1). The strong signal causes spectral leakage in fast Fourier transforms (FFT) even though a Hann window taper was applied before the FFT. However, it does not influence our inversion as the frequency range is small.

#### 4.2. Velocity Inversion

Most previous surface wave inversion studies treat the subsurface as a layered model with either fixed or variable layer thickness (for two-station (Yudistira et al., 2017) or multi-station (Cheng et al., 2015; Xia et al., 1999) surveys). The firn layer is defined as a layer with continuous metamorphism of snow to ice, which results in a smooth increase of  $P$ - and  $S$ - velocity and density as a function of depth (King & Jarvis, 2007; Schlegel et al., 2019), until it becomes near constant beneath  $\sim 100$  m at Rutford Ice Stream. We therefore use a near-continuous model of 100 layers, each with a layer thickness of 1 m, over a half-space at the bottom of the model.

To simulate the phase velocity dispersion of the Rayleigh wave we use the Python package *disba* (Luu, 2021), which was translated from the well-adopted Fortran program *surf96* from Computer Programs in Seismology (Herrmann, 2013). With a 100-layer model, we significantly increase the number of variables and the non-uniqueness of the inversion. A Gaussian-Newton inversion procedure is applied using the package *pyGimli* (Rücker et al., 2017), with the regularization  $\lambda$  to be 20, and a predefined relative error of 10% to prevent

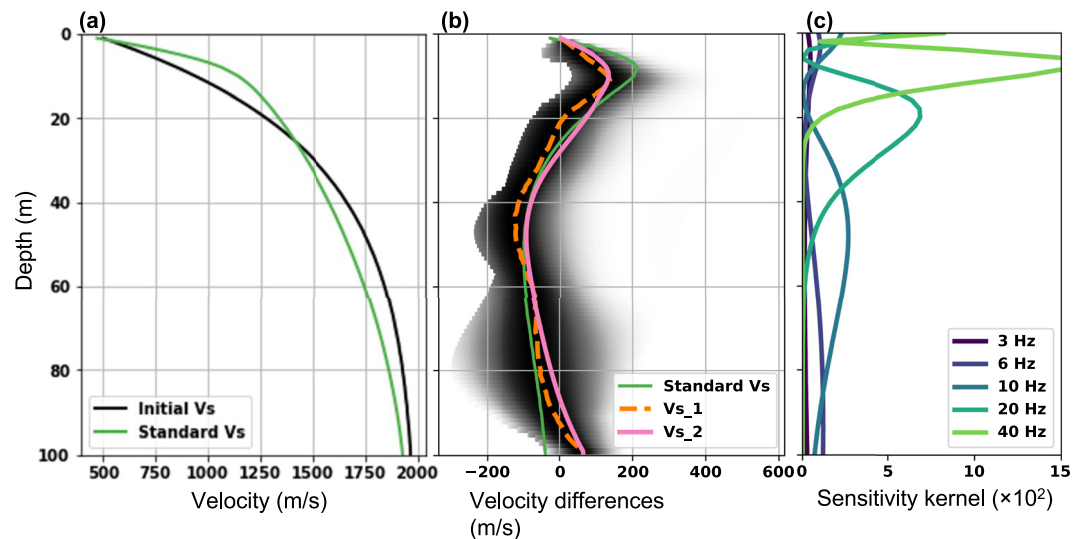


**Figure 6.** (a) The initial smooth  $V_s$  model. The  $V_s$  profile derived from the standard  $V_p$  refraction experiment (named standard  $V_s$ ). (b) Velocity differences between Inverted  $V_s$  models and the initial model,  $V_{s\_1}$  from maximal probability density function (greyscale) and  $V_{s\_2}$  from direct inversion of a fully selective stacked Cross-correlations (CCs) virtual shot gather. (c) Sensitivity kernel calculated from the inverted model  $V_{s\_1}$ .

overfitting. The large relative error and regularization also means that we find a solution which is close to the starting model.

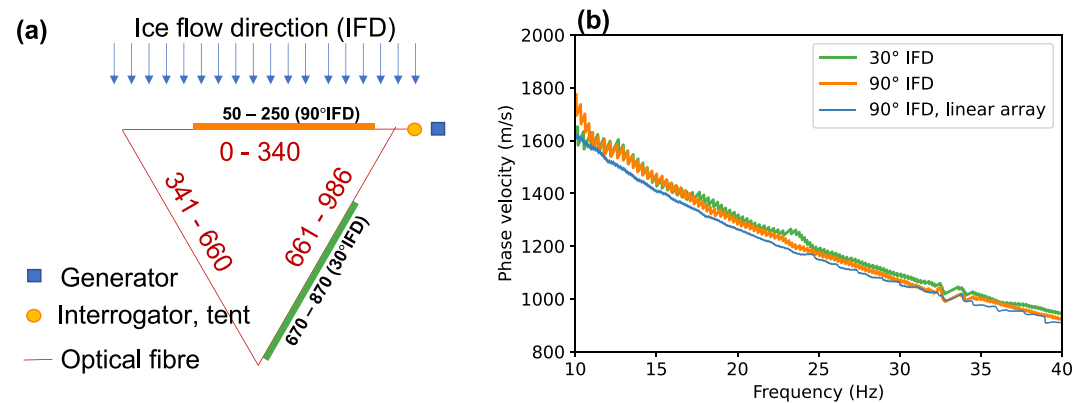
To provide a realistic starting model we applied the WHB inversion to the refraction data set acquired previously and used by Smith et al. (2015) to obtain a  $V_p$ -depth model (Figure 1c). Then assuming a constant  $V_p/V_s = 1.95$  (Smith et al., 2015), we obtained a  $V_s$  model. We name this model the “standard  $V_s$ ” and use it as a comparison to our surface wave inverted models. The starting model for the inversion is a smoothed version of the standard  $V_s$ . The general trend of the standard  $V_s$  model is preserved but the “kink” at around 9 m is smeared (Figure 6a). Figure 6b highlights the differences between the standard  $V_s$  model and the starting model, which shows that the standard  $V_s$  model has a higher value from 0 to  $\sim 25$  m and lower value from  $\sim 25$  to 100 m.

Figure 5c shows that the initial model is generally consistent in phase velocity with that obtained from the data. At higher frequencies, the starting model has lower phase velocity than the data, which indicates the starting model underestimates the phase velocity at shallow depths.

To capture the uncertainty in the data, we calculate the CCs for 3 geophones (1 co-located, and 2 in-line with the DAS cable). For each virtual source, we produce 9 dispersion curves, by dividing the 453 selected CCs into 9 groups for stacking. This process results in 27 ( $9 \times 3$ ) dispersion curves (Figure S8 in Supporting Information S1). We then invert all 27 dispersion curves for  $S$ -wave velocity profiles. Lastly, a probability density function (PDF) is calculated for each layer over its 27 measurements. The maximal point of PDFs, for each layer, represents a final  $V_s$  profile ( $V_{s\_1}$ ). In Figure 6b, we present the inverted  $V_{s\_1}$  after subtracting the starting model, with the amplitudes of PDFs presented as greyscale. See Figure S3 in Supporting Information S1 for further details of the process.

Alternatively, a  $V_s$  ( $V_{s\_2}$  in Figure 6b) is directly inverted from the passive dispersion curve in Figure 5c which is extracted from the Rayleigh wave response of fully stacked CCs (all the 453 selected time spans and 3 virtual sources).

As highlighted in Figure 6b, the  $V_{s\_1}$  profile is almost overlapping with the  $V_{s\_2}$  profile from 0 to 14 m, while the two profiles differ slightly at depths below 14 m, further indicating uncertainties of the final models. In general, our two  $V_s$  models agree with the standard  $V_s$  down to 80 m depth. Below 80 m depth, our models suggest a slightly steeper increase in velocity compared to the standard  $V_s$ , reaching up to 100 m/s higher than the initial model. In both our  $V_s$  models and the standard model we see a clear peak (largest difference with the initial model) at around 9 m (standard  $V_s$ ) to 12 m ( $V_{s\_1}$ ) depth, which is similar to the densification observation and modeled by the regional atmospheric climate model by van den Broeke (2008), across West Antarctica.



**Figure 7.** (a) Schematic of the geometry of the triangle Distributed Acoustic Sensing (DAS) array, with a loop of 986 m. The thick lines indicating two 200 m DAS segments have been used for the seismic noise interferometry study. (b) Dispersion curves were obtained from the two segments which are close to the interrogator indicated as 90° ice flow direction (IFD) (ice flow direction) and 30° IFD. The result from the linear array is also plotted.

Sensitivity analysis is done at discrete frequencies (3, 6, 10, 20, and 40 Hz) using the inverted Versus\_1 model (Figure 6c). This indicates that the highest sensitivity of most signals (>20 Hz) is over the 0–40 m depth range. Signals below 10 Hz have greater sensitivity over the lower part of the model. Below 6 Hz, the Rayleigh wave is most sensitive to the lowermost layer of our model, which is assumed to be a half-space.

### 4.3. Is the Firn Layer Seismically Anisotropic?

Clear azimuthal anisotropy has been reported at Rutford Ice Stream by Harland et al. (2013) and Smith et al. (2017), with the fast *S*-wave direction perpendicular (90°) to the ice flow direction (IFD). Hudson et al. (2021) also observed strong shear wave splitting in icequake signals recorded by DAS. These seismic experiments do not provide constraints on the depth distribution of the anisotropic ice, as the measurements integrate over the entire wave path from the icequake hypocenter at the ice-bed interface to the surface receivers. However, using polarimetric radar measurements, Jordan et al. (2022) report near-surface azimuthal anisotropy on Rutford Ice Stream, although their measurements are not coincident with this experiment.

We investigate the feasibility of imaging anisotropy with CCs of surface waves retrieved from different azimuths. We use a DAS array in a triangular configuration and assume a laterally homogenous firn layer. As shown in Figure 7a, we take two segments of the triangular array (channel 50–250 and channel 670–870). We chose channels 670–870, with a larger distance to the interrogator and the generator, to reduce the angle between the ray path and the DAS cable. Since the snowmobile traveling to the generator is the dominant high-frequency seismic noise source, we could not retrieve a stable Rayleigh wave response from the third segment that is perpendicular to the wave propagation direction.

With virtual sources at DAS channels 150 and 750, respectively, we calculate and selectively stack CCs for each segment (Figures S9a and S9b in Supporting Information S1). A higher selection threshold of 0.01 is chosen as the DAS CCs are in general of higher amplitude than DAS-geophone CCs. Dispersion curves of the two segments are then calculated from the *f*-*k* domain (Figures S9c and S9d in Supporting Information S1), as with the linear-array study. In Figure 7b we show the two dispersion curves together with the result from the linear array. Note the linear array result is more stable due to the involvement of geophone data. The difference between the triangle array 90° IFD dispersion curve and the linear array result might indicate a slight horizontal heterogeneity in the firn layer. Horizontal heterogeneity might also exist between the two sides of the triangle. When comparing the two dispersion curves from the triangle array we see that they are in general nearly overlapping with each other from 10 to 27 Hz. For above 27 Hz, the 30° IFD curve indicates a slightly higher phase velocity, but the difference is small compared with the measurement uncertainties. At around 24 and 33 Hz there are artifacts from the *f*-*k* transform. In this study, neither the heterogeneity or the anisotropy effect produces a notable dispersion curve difference between the 30° IFD and 90° IFD. Thus, it suggests that the firn layer, above ~80 m depth (for the signals above 10 Hz), is likely not strongly azimuthally anisotropic. Additionally, we note that

our measurements here have large uncertainty and that we cannot rule out a VTI anisotropy in the firn layer. A comparison of Rayleigh and Love wave derived shear-velocities would provide a means of testing this.

## 5. Discussion

In this study, we investigate the use of noise data recorded by DAS, deployed on Rutford Ice Stream, West Antarctica, to obtain a high-resolution shear wave velocity profile of the firn. We compare CCs calculated over 5 days using a single DAS channel as a virtual source against the use of three geophones (collocated or near collocated) as the virtual sources. A superior SNR is obtained with a geophone virtual source. The coherence of instantaneous instrument noise over all the DAS channels degrades the cross-correlations, whilst introducing a geophone as a virtual source breaks down that coherence of the instrument noise.

Stable Rayleigh wave responses are retrieved from CCs between vertical component geophone data and horizontal component DAS data, as a result of the Rayleigh wave elliptical particle motion. We notice, however, that there are phase shifts introduced by: (a) the elliptical particle motion produces a 90° phase shift between vertical and horizontal particle motions, (b) the difference between particle motion velocity and strain rate, and (c) the difference in instrument responses. However, these do not inhibit the dispersion analysis, as it uses only the slope to calculate dispersion curves. We note that for studying waves other than Rayleigh waves, it might be beneficial to consider using the horizontal component parallel with the cable. We deliberately chose to use the vertical component to demonstrate the applicability of the hybrid instrument approach, because vertical component geophones are widely used for near-surface imaging applications.

The noisy Rayleigh wave response from using a DAS channel as a virtual source is likely due to the instrument noise on DAS channels having a destructive impact on the CCs. First, we can see clear horizontal bands in Figure 3a which are most dominant at  $t = 0$ , and therefore indicate that the instrument noise on each DAS channel is not independent. This is likely due to the nature of DAS measurement that senses the entire cable with a single interrogator unit, which results in such common mode noise (Lindsey et al., 2020), as shown in Figure S4e in Supporting Information S1. When a geophone is used as the virtual source, it breaks the coherency of this instrumental noise. Additionally, we observe that the dominant seismic noise contributing to the seismic responses is transient in nature, therefore a large number of CCs derived from a DAS virtual source contain only instrument noise.

Based on our results we argue that deploying DAS together with conventional seismic instruments (hybrid instrumentation) would be beneficial. This is consistent with previous studies, such as: combining seismometer and DAS for calculating receiver function and surface wave dispersion (Yu et al., 2019); converting strain to particle velocity or calibrating the conversion (Lindsey et al., 2020; Porritt et al., 2022; van den Ende & Ampuero, 2021), or to apply the H/V method between DAS and vertical component of a seismometer (Spica, Pertou, et al., 2020).

Selective stacking is applied to improve CCs. Only 453 out of 3,068 2-min CCs panels are selected and stacked for shear wave inversions. The CCs are picked in the tau-p domain based on the maximal amplitude, for simplicity. While a signal-noise-ratio criterion (i.e., maximal amplitude divided by maximal amplitude away from zero delay time (e.g.,  $< -0.5$  or  $> 0.5$  s)) could be investigated in future studies. With selective stacking we eliminate a large amount of data containing only instrument noise. The selected CCs contain mostly high-frequency signals from the snowmobile or transient low-frequency surface wave events. The snowmobile was used to approach the generator location in-line with the linear fiber optic cable array, 50 m away from the interrogator (Figure 7a), which produces surface wave noise that is mostly in the stationary phase zone (Snieder, 2004) traveling near-parallel to the fiber. The (suspected) crevassing generated surface wave signals are mostly from the shear margin of the ice stream (Figure S5 in Supporting Information S1), although not homogeneously distributed, they are generally in-line with the fiber optic cable. Additionally, the criterion on apparent velocity for selective stacking also helps to remove signals from the non-stationary phase zone. Note that noise sources in the non-stationary phase can also provide important Earth structure information when the noise sources and earth structure are jointly inverted (Fichtner et al., 2016).

The dispersion curves obtained from the passive and active datasets show strong agreement over the frequency range of 10–50 Hz. While the hammer and plate source surveys produce energy down to 10 Hz, it is most stable above 15 Hz, which could provide a reliable S velocity profile down to ~60 m (Figure 6). The SI extends the reliable measurement range down to 3 Hz, which enables an inversion over the entire column of the firn layer.

We did not observe clear ocean wave induced primary or secondary microseism noise, as observed as the dominant ambient noise on broadband seismometers from 0.01 to 1 Hz (Bensen et al., 2007). Previous studies with submarine DAS cables have recorded the microseism from 0.2 to 2 Hz (Sladen et al., 2019) and down to 0.5 Hz (Cheng et al., 2015; Spica, Nishida, et al., 2020). Some onshore studies also suggest the abundance of low-frequency noise with noise power spectrum analysis (Hudson et al., 2021; Lindsey et al., 2020). It is, however, shown in our study that the DAS signals below 1 Hz are likely wind-related, which is most likely due to the shallow burial depth of the cable. It is also possible that the linear fiber is insensitive to microseism signals because of its propagation direction near perpendicular to the fiber.

The *S*-wave velocity profile obtained from this study fits well with the velocity profile inverted from a standard refraction *P*-wave experiment conducted in the BEAMISH project (Smith et al., 2021), assuming a  $V_p/V_s$  ratio of 1.95 (Smith et al., 2015) at depths of 0–80 m. Below 80 m the profiles from the methods diverge, with higher  $V_s$  at depths greater than 80 m from the surface wave inversion. This may suggest a decrease of the  $V_p/V_s$  ratio at depth, or an increase in azimuthal anisotropy. However, at these depths, the reliability of the standard refraction results decreases due to the data offset limitation of  $\sim 1$  km. Also, spatial heterogeneity cannot be ruled out as the surveys are not collocated. Nevertheless, the shape and form of the inverted  $V_s$  profiles show good agreement with the refraction survey, with both methods showing a velocity-depth gradient change at around 12 m. This feature of the velocity profile indicates the depth of the critical density, marking the transition between the first two stages of the densification process (Herron & Langway, 1980). Above this depth, the dominant compaction mechanism is grain settling and packing and exhibits the highest densification rate. Below this transition progression to pore close-off occurs with a lower rate of densification. The velocity-depth gradients above and below this depth agree with this interpretation. This agreement between the methods, reproducing the velocity gradient transition at similar depths is significant. The standard refraction WHB method uses a double exponential fit to the travel-times (Kirchner & Bentley, 1979) which can force the presence of this gradient change when a simple polynomial fitting method may not. The results from noise interferometry and surface wave inversion, therefore, verify the assumption of the double exponential fitting step at this site and provide an independent and robust measure of this critical density transition in the firn profile.

With a triangular fiber optic array, we retrieve Rayleigh wave responses along  $90^\circ$  and  $30^\circ$  from the ice flow direction. We find a small difference between the two dispersion curves from 10 to 40 Hz. Considering uncertainties in the measurements, it qualitatively indicates no strong azimuthal anisotropy in the upper 80 m (the dominant sensitivity of this frequency band is the top 80 m (Figure 6b)). However, polarimetric radar measurements of Jordan et al. (2022) indicate azimuthal anisotropy at depths of 40–100 m across Rutford Ice Stream. Laterally, they find weaker anisotropy in the ice stream center (less deformation) than toward the shear margin. Our measurements of the azimuthal variation of the Rayleigh wave-phase velocity contain uncertainties that may be due to lateral heterogeneity in the firn layer or instability of the cross-correlation functions. But within that uncertainty, our measurements are consistent with the Jordan et al. (2022) results and preclude strong azimuthal anisotropy at the center of the ice stream.

Our measurements of  $V_s$  complement those of  $V_p$ , without requiring additional *S*-wave sources or 3-component sensors. The method uses DAS, collocated vertical component geophones, and natural seismic signals from crevasses and noise from snowmobiles, which means it could be convenient for the deployment and might be a feasible method for large-scale firn imaging. This may lead to an improved understanding of the mechanical properties of the firn and their variation. Although standard refraction methods can be adapted to derive a  $V_s$  profile, with *S*-wave sources and three component instruments (King & Jarvis, 2007; Kirchner & Bentley, 1990), in general, only  $V_p$  profiles are measured. Efforts were made to reproduce the standard *P*-wave refraction survey method using diving *P*-waves from a hammer and plate source with DAS recording. However, inherent to the DAS method, a combination of the effects of gauge length and spatial averaging near the shot location, hinders the derivation of a well resolved velocity profile. Nevertheless, our study suggests that DAS measurements and surface wave inversion have the potential to upscale for the investigation of firn properties over large areas.

Another potential benefit of the method presented here compared to the standard seismic refraction method is the capacity of the surface wave (passive or active) to image low-velocity layers (Zhang et al., 2007). The seismic refraction method would fail in the presence of low-velocity layers as no rays will undergo critical refraction at the top of it (base of the ice layer). This situation may arise where melt has occurred and refreezing produces ice lenses overlying lower velocity firn layers, as for example, reported on Larsen C Ice Shelf (Ashmore et al., 2017).

Although the  $V_s$  profile in our study is inverted from noise CCs, we observe consistency between CC retrieved dispersion and active shot dispersion, which suggests the inversion methods would work with active seismic data as well. A source producing lower frequencies (e.g., explosives or weight drop) would allow greater depth penetration. Since Rayleigh wave signals are naturally acquired in conventional refraction surveys, revisiting these data with our method could provide an independent measurement of  $V_s$  and might yield new insights.

## 6. Conclusions

Applying noise interferometry to DAS data, we retrieved broadband (3–50 Hz) and stable CCs representing Rayleigh wave responses traveling along the DAS fiber. We show that the SNR improves when using a collocated geophone as the virtual source or selective stacking of only the best CCs (selection based on the tau-p domain). Seismic noise sources are found to be transient and include lower-frequency (2–10 Hz) surface wave signals from the shear margins of the ice stream, and high-frequency noise up to 80 Hz from a snowmobile. The Rayleigh wave dispersion curves are validated using active shot gathers.

Inverting the dispersion curves, we produce an  $S$ -wave velocity ( $V_s$ ) profile of the firn layer, which resolves a “kink” at 12 m depth, corresponding to the critical density where the mode of firn compaction changes. This model shows good agreement with a standard  $V_p$  refraction derived model. No significant azimuthal anisotropy is observed in the upper 80 m, using 10–40 Hz signal, which is consistent with previous studies which indicate that along the center of the ice stream the top of the firn layer is not undergoing strong horizontal deformation.

Our study demonstrates that the use of surface waves, retrieved from DAS SI, could complement the refraction  $V_p$  profiles for studies of the firn layer. Since the acquisitions of DAS and seismic noise are simpler than geophone refraction surveying, these measurements have the potential to upscale to large areas of the ice sheets. This in turn might help decrease the uncertainty of mass balance estimation and palaeoclimate studies. Additionally, using surface waves instead of refraction waves will potentially allow investigation of the firn column where standard refraction methods fail, for example, in the presence of low velocity layers such as those observed on lower-latitude ice shelves. Finally, the methodology that we have developed can be easily applied to imaging the near surface in a host of other environmental applications where fiber optic cables can be deployed; examples include landslide monitoring, levee and embankment assessment, and sinkhole studies.

### Acknowledgments

This work was funded by the UK's Department for Business, Energy and Industrial Strategy through the DigiMon ACT CCS project (project number 299622), and the NERC Collaborative Antarctic Science Scheme grant (Grant CASS-166). Fieldwork was undertaken as part of the BEAMISH Project (NERC AFI award numbers NE/G014159/1). We thank Silixa for the loan of an iDAS interrogator. Geophones were borrowed from the UK Geophysical Equipment Facility (GEF loan number 1111). This work used computational facilities of the Advanced Computing Research Centre, University of Bristol - <http://www.bristol.ac.uk/acrc/>. Obspy (Krischer et al., 2015) is intensively used for data processing. The tau-p transform was performed with PyLops (Ravasi & Vasconcelos, 2020). Jelle Assink (KNMI) is thanked for useful discussion on the low-frequency signal in DAS and pointing out the weather data from ECMWF (European Centre for Medium-Range Weather Forecasts, 2017). Thomas Hudson and Sacha Lapins are thanked for useful discussions. Hanneke Paulssen is thanked for reading and commenting on the manuscript. We thank Emma Smith, Andreas Fichtner, two anonymous reviewers and the associated editor Paul Winberry for their constructive comments.

### Data Availability Statement

Seven hours of continuous DAS data (decimated to 10 m channel distance and 100 Hz sampling rate), and continuous geophones data (3 collocated geophone, A000, R102, R104, vertical component) have been made available through Zenodo (Zhou et al., 2022), which could be used to reproduce the SI and surface wave inversion for  $S$ -wave velocity profile.

### References

- Ajo-Franklin, J. B., Dou, S., Lindsey, N. J., Monga, I., Tracy, C., Robertson, M., et al. (2019). Distributed acoustic sensing using dark fiber for near-surface characterization and broadband seismic event detection. *Scientific Reports*, 9(1), 1328. <https://doi.org/10.1038/s41598-018-36675-8>
- Alley, R. B. (1987). Firn densification by grain-boundary sliding: A first model. *Journal de Physique Colloques*, 48(C1), 249–256. <https://doi.org/10.1051/jphyscol:1987135>
- Ashmore, D. W., Hubbard, B., Luckman, A., Kulessa, B., Bevan, S., Booth, A., et al. (2017). Ice and firn heterogeneity within Larsen C Ice Shelf from borehole optical televiewing. *Journal of Geophysical Research: Earth Surface*, 122(5), 1139–1153. <https://doi.org/10.1002/2016JF004047>
- Bensen, G. D., Ritzwoller, M. H., Barmin, M. P., Levshin, A. L., Lin, F., Moschetti, M. P., et al. (2007). Processing seismic ambient noise data to obtain reliable broad-band surface wave dispersion measurements. *Geophysical Journal International*, 169(3), 1239–1260. <https://doi.org/10.1111/j.1365-246X.2007.03374.x>
- Booth, A. D., Christoffersen, P., Schoonman, C., Clarke, A., Hubbard, B., Law, R., et al. (2020). Distributed acoustic sensing of seismic properties in a borehole drilled on a fast-flowing Greenlandic outlet glacier. *Geophysical Research Letters*, 47(13), e2020GL088148. <https://doi.org/10.1029/2020GL088148>
- Brisbourne, A. M., Kendall, M., Kufner, S. K., Hudson, T. S., & Smith, A. M. (2021). Downhole distributed acoustic seismic profiling at Skytrain Ice Rise, West Antarctica. *The Cryosphere*, 15(7), 3443–3458. <https://doi.org/10.5194/tc-15-3443-2021>
- Butcher, A., Hudson, T., Kendall, J., Kufner, S., Brisbourne, A., & Stork, A. (2021). Radon transform-based detection of microseismicity on DAS networks: A case study from Antarctica. In *EAGE GeoTech 2021—1st EAGE workshop on induced seismicity*. <https://doi.org/10.3997/2214-4609.202131039>

- Butcher, A., Stork, A. L., Verdon, J. P., Kendall, J. M., Plenkens, K., Booth, F., et al. (2021). Evaluating rock mass disturbance within open-pit excavations using seismic methods: A case study from the Hinkley point C nuclear power station. *Journal of Rock Mechanics and Geotechnical Engineering*, 13(3). <https://doi.org/10.1016/j.jrmge.2020.12.001>
- Case, E., & Kingslake, J. (2022). Phase-sensitive radar as a tool for measuring firn compaction. *Journal of Glaciology*, 68(267), 139–152. <https://doi.org/10.1017/jog.2021.83>
- Chaput, J., Aster, R., Karplus, M., & Nakata, N. (2022). Ambient high-frequency seismic surface waves in the firn column of central West Antarctica. *Journal of Glaciology*, 68(270), 1–14. <https://doi.org/10.1017/jog.2021.135>
- Cheng, F., Chi, B., Lindsey, N. J., Dawe, T. C., & Ajo-Franklin, J. B. (2021). Utilizing distributed acoustic sensing and ocean bottom fiber optic cables for submarine structural characterization. *Scientific Reports*, 11(1), 5613. <https://doi.org/10.1038/s41598-021-84845-y>
- Cheng, F., Xia, J., Behm, M., Hu, Y., & Pang, J. (2019). Automated data selection in the Tau-p domain: Application to passive surface wave imaging. *Surveys in Geophysics*, 40(5), 1211–1228. <https://doi.org/10.1007/s10712-019-09530-2>
- Cheng, F., Xia, J., Luo, Y., Xu, Z., Wang, L., Shen, C., et al. (2016). Multichannel analysis of passive surface waves based on cross correlations. *Geophysics*, 81(5), EN57–EN66. <https://doi.org/10.1190/geo2015-0505.1>
- Cheng, F., Xia, J., Xu, Y., Xu, Z., & Pan, Y. (2015). A new passive seismic method based on seismic interferometry and multichannel analysis of surface waves. *Journal of Applied Geophysics*, 117, 126–135. <https://doi.org/10.1016/j.jappgeo.2015.04.005>
- Correa, J., Freifeld, B. M., Revzner, R., Wood, T., Tertyshnikov, K., & Bona, A. (2018). Continuous DAS VSP monitoring using surface orbital vibrators: Field trials for optimal configuration at the CO2CRC Otway Project. In *80th EAGE conference and exhibition 2018 workshop programme, cp-00040*. <https://doi.org/10.3997/2214-4609.201801917>
- Craig, H., Horibe, Y., & Sowers, T. (1988). Gravitational separation of gases and isotopes in polar ice caps. *Science*, 242(4886), 1675–1678. <https://doi.org/10.1126/science.242.4886.1675>
- Cuffey, K. M., & Paterson, W. S. B. (2010). *The physics of glaciers* (4th ed.). Butterworth-Heinemann.
- Diebold, J. B., & Stoffa, P. L. (1981). The traveltimes equation, tau-p mapping, and inversion of common midpoint data. *Geophysics*, 46(3), 238–254. <https://doi.org/10.1190/1.1441196>
- Diez, A., Bromirski, P. D., Gerstoft, P., Stephen, R. A., Anthony, R. E., Aster, R. C., et al. (2016). Ice shelf structure derived from dispersion curve analysis of ambient seismic noise, Ross Ice Shelf, Antarctica. *Geophysical Journal International*, 205(2), 785–795. <https://doi.org/10.1093/gji/ggw036>
- Dou, S., Lindsey, N., Wagner, A. M., Daley, T. M., Freifeld, B., Robertson, M., et al. (2017). Distributed acoustic sensing for seismic monitoring of the near surface: A traffic-noise interferometry case study. *Scientific Reports*, 7(1), 11620. <https://doi.org/10.1038/s41598-017-11986-4>
- European Centre for Medium-Range Weather Forecasts. (2017). *ERA5 reanalysis*. Research Data Archive at the National Center for Atmospheric Research, Computational and Information Systems Laboratory. <https://doi.org/10.5065/D6X34W69>
- Fichtner, A., Stehly, L., Ermert, L., & Boehm, C. (2016). Generalized interferometry—I: Theory for interstation correlations. *Geophysical Journal International*, 208(2), 603–638. <https://doi.org/10.1093/gji/ggw420>
- Harland, S. R., Kendall, J. M., Stuart, G. W., Lloyd, G. E., Baird, A. F., Smith, A. M., et al. (2013). Deformation in Rutford Ice Stream, West Antarctica: Measuring shear-wave anisotropy from icequakes. *Annals of Glaciology*, 54(64), 105–114. <https://doi.org/10.3189/2013AoG64A033>
- Herrmann, R. B. (2013). Computer programs in seismology: An evolving tool for instruction and research. *Seismological Research Letters*, 84(6), 1081–1088. <https://doi.org/10.1785/S00220110096>
- Herron, M. M., & Langway, C. C. (1980). Firn densification: An empirical model. *Journal of Glaciology*, 25(93), 373–385. <https://doi.org/10.1017/S0022143000015239>
- Hollmann, H., Treverrow, A., Peters, L. E., Reading, A. M., & Kulesa, B. (2021). Seismic observations of a complex firn structure across the Amery Ice Shelf, East Antarctica. *Journal of Glaciology*, 67(265), 777–787. <https://doi.org/10.1017/jog.2021.21>
- Hudson, T. S., Baird, A. F., Kendall, J. M., Kufner, S. K., Brisbourne, A. M., Smith, A. M., et al. (2021). Distributed acoustic sensing (DAS) for natural microseismicity studies: A case study from Antarctica. *Journal of Geophysical Research: Solid Earth*, 126(7). <https://doi.org/10.1029/2020JB021493>
- Ide, S., Araki, E., & Matsumoto, H. (2021). Very broadband strain-rate measurements along a submarine fiber-optic cable off Cape Muroto, Nankai subduction zone, Japan. *Earth Planets and Space*, 73(1), 63. <https://doi.org/10.1186/s40623-021-01385-5>
- Jordan, T. M., Martín, C., Brisbourne, A. M., Schroeder, D. M., & Smith, A. M. (2022). Radar characterization of ice crystal orientation fabric and anisotropic viscosity within an Antarctic Ice Stream. *Journal of Geophysical Research: Earth Surface*, 127(6), e2021GL097070. <https://doi.org/10.1029/2022jef006673>
- Jordan, T. M., Schroeder, D. M., Elsworth, C. W., & Siegfried, M. R. (2020). Estimation of ice fabric within Whillans Ice Stream using polarimetric phase-sensitive radar sounding. *Annals of Glaciology*, 61(81), 74–83. <https://doi.org/10.1017/aog.2020.6>
- King, E. C., & Jarvis, E. P. (2007). Use of shear waves to measure Poisson's ratio in polar firn. *Journal of Environmental & Engineering Geophysics*, 12(1), 15–21. <https://doi.org/10.2113/JEEG12.1.15>
- Kirchner, J. F., & Bentley, C. R. (1979). Seismic Short-refraction studies on the Ross Ice Shelf, Antarctica. *Journal of Glaciology*, 24(90), 313–319. <https://doi.org/10.3189/S0022143000014830>
- Kirchner, J. F., & Bentley, C. R. (1990). Riggs III: Seismic short-refraction studies using an analytical curve-fitting technique (pp. 109–126). <https://doi.org/10.1029/AR042p0109>
- Krischer, L., Megies, T., Barsch, R., Beyreuther, M., Lecocq, T., Caudron, C., & Wassermann, J. (2015). ObsPy: A bridge for seismology into the scientific Python ecosystem. *Computational Science & Discovery*, 8(1), 014003. <https://doi.org/10.1088/1749-4699/8/1/014003>
- Kufner, S., Brisbourne, A. M., Smith, A. M., Hudson, T. S., Murray, T., Schlegel, R., et al. (2021). Not all icequakes are created equal: Basal icequakes suggest diverse bed deformation mechanisms at Rutford Ice Stream, West Antarctica. *Journal of Geophysical Research: Earth Surface*, 126(3). <https://doi.org/10.1029/2020JF006001>
- Lellouch, A., Yuan, S., Spica, Z., Biondi, B., & Ellsworth, W. L. (2019). Seismic velocity estimation using passive downhole distributed acoustic sensing records: Examples from the San Andreas Fault observatory at depth. *Journal of Geophysical Research: Solid Earth*, 124(7), 6931–6948. <https://doi.org/10.1029/2019JB017533>
- Lindner, F., Laska, G., Walter, F., & Doran, A. K. (2019). Crevasse-induced Rayleigh-wave azimuthal anisotropy on glacier de la Plaine Morte, Switzerland. *Annals of Glaciology*, 60(79), 96–111. <https://doi.org/10.1017/aog.2018.25>
- Lindsey, N. J., Rademacher, H., & Ajo-Franklin, J. B. (2020). On the broadband instrument response of fiber-optic DAS arrays. *Journal of Geophysical Research: Solid Earth*, 125(2), 1–16. <https://doi.org/10.1029/2019JB018145>
- Lior, I., Mercerat, E. D., Rivet, D., Sladen, A., & Ampuero, J.-P. (2022). Imaging an underwater basin and its resonance modes using optical fiber distributed acoustic sensing. *Seismological Research Letters*, 93(3), 1573–1584. <https://doi.org/10.1785/S00220210349>
- Lior, I., Sladen, A., Rivet, D., Ampuero, J., Hello, Y., Becerril, C., et al. (2021). On the detection capabilities of underwater distributed acoustic sensing. *Journal of Geophysical Research: Solid Earth*, 126(3), 1–20. <https://doi.org/10.1029/2020JB020925>



- Luu, K. (2021). disba: Numba-accelerated computation of surface wave dispersion. *Zenodo*. <https://doi.org/10.5281/zenodo.3987395>
- Mateeva, A., Lopez, J., Chalenski, D., Tatanova, M., Zwartjes, P., Yang, Z., et al. (2017). 4D das VSP as a tool for frequent seismic monitoring in deep water. *The Leading Edge*, *36*(12), 995–1000. <https://doi.org/10.1190/tle36120995.1>
- Morris, E. M., Mulvaney, R., Arthern, R. J., Davies, D., Gurney, R. J., Lambert, P., et al. (2017). Snow densification and recent accumulation along the iSTAR traverse, Pine Island Glacier, Antarctica. *Journal of Geophysical Research: Earth Surface*, *122*(12), 2284–2301. <https://doi.org/10.1002/2017j004357>
- Murray, T., Smith, A. M., King, M. A., & Weedon, G. P. (2007). Ice flow modulated by tides at up to annual periods at Rutford Ice Stream, West Antarctica. *Geophysical Research Letters*, *34*(18), L18503. <https://doi.org/10.1029/2007GL031207>
- Olivier, G., Bagnier, F., Campillo, M., Lynch, R., & Roux, P. (2015). Body-wave reconstruction from ambient seismic noise correlations in an underground mine. *Geophysics*, *80*(3), KS11–KS25. <https://doi.org/10.1190/geo2014-0299.1>
- Park, C., Miller, R., Laflen, D., Bennett, B., Ivanov, J., Neb, C., & Huggins, R. (2004). Imaging dispersion curves of passive surface waves. 2004 SEG Annual Meeting.
- Park, C. B., Miller, R. D., & Xia, J. (1999). Multichannel analysis of surface waves. *Geophysics*, *64*(3), 800–808. <https://doi.org/10.1190/1.1444590>
- Peters, L. E., Anandakrishnan, S., Alley, R. B., Winberry, J. P., Voigt, D. E., Smith, A. M., & Morse, D. L. (2006). Subglacial sediments as a control on the onset and location of two Siple Coast ice streams, West Antarctica. *Journal of Geophysical Research*, *111*(B1), B01302. <https://doi.org/10.1029/2005jb003766>
- Picotti, S., Vuan, A., Carcione, J. M., Horgan, H. J., & Anandakrishnan, S. (2015). Anisotropy and crystalline fabric of Whillans Ice Stream (West Antarctica) inferred from multicomponent seismic data. *Journal of Geophysical Research: Solid Earth*, *120*(6), 4237–4262. <https://doi.org/10.1002/2014jb011591>
- Porritt, R., Abbott, R., & Poppeliers, C. (2022). Quantitative assessment of distributed acoustic sensing at the source physics experiment, phase II. <https://doi.org/10.2172/1855336>
- Ravasi, M., & Vasconcelos, I. (2020). PyLops—A linear-operator Python library for scalable algebra and optimization. *SoftwareX*, *11*, 100361. <https://doi.org/10.1016/j.softx.2019.100361>
- Riverman, K. L., Alley, R. B., Anandakrishnan, S., Christianson, K., Holschuh, N. D., Medley, B., et al. (2019). Enhanced firn densification in high-accumulation shear margins of the NE Greenland ice stream. *Journal of Geophysical Research: Earth Surface*, *124*(2), 365–382. <https://doi.org/10.1029/2017JF004604>
- Rodríguez Tribaldos, V., & Ajo-Franklin, J. B. (2021). Aquifer monitoring using ambient seismic noise recorded with distributed acoustic sensing (DAS) deployed on dark fiber. *Journal of Geophysical Research: Solid Earth*, *126*(4), 1–20. <https://doi.org/10.1029/2020jb021004>
- Rücker, C., Günther, T., & Wagner, F. M. (2017). pyGIMLI: An open-source library for modelling and inversion in geophysics. *Computers & Geosciences*, *109*, 106–123. <https://doi.org/10.1016/j.cageo.2017.07.011>
- Scambos, T. A., Haran, T. M., Fahnestock, M. A., Painter, T. H., & Bohlander, J. (2007). MODIS-based Mosaic of Antarctica (MOA) data sets: Continent-wide surface morphology and snow grain size. *Remote Sensing of Environment*, *111*(2–3), 242–257. <https://doi.org/10.1016/j.rse.2006.12.020>
- Schimmel, M., & Paulssen, H. (1997). Noise reduction and detection of weak, coherent signals through phase-weighted stacks. *Geophysical Journal International*, *130*(2), 497–505. <https://doi.org/10.1111/j.1365-246X.1997.tb05664.x>
- Schimmel, M., Stutzmann, E., & Gallart, J. (2011). Using instantaneous phase coherence for signal extraction from ambient noise data at a local to a global scale. *Geophysical Journal International*, *184*(1), 494–506. <https://doi.org/10.1111/j.1365-246X.2010.04861.x>
- Schlegel, R., Diez, A., Löwe, H., Mayer, C., Lambrecht, A., Freitag, J., et al. (2019). Comparison of elastic moduli from seismic diving-wave and ice-core microstructure analysis in Antarctic polar firn. *Annals of Glaciology*, *60*(79), 220–230. <https://doi.org/10.1017/aog.2019.10>
- Sergeant, A., Chmiel, M., Lindner, F., Walter, F., Roux, P., Chaput, J., et al. (2020). On the Green's function emergence from interferometry of seismic wave fields generated in high-melt glaciers: Implications for passive imaging and monitoring. *The Cryosphere*, *14*(3), 1139–1171. <https://doi.org/10.5194/tc-14-1139-2020>
- Shapiro, N. M., & Campillo, M. (2004). Emergence of broadband Rayleigh waves from correlations of the ambient seismic noise. *Geophysical Research Letters*, *31*(7), 8–11. <https://doi.org/10.1029/2004GL019491>
- Shapiro, N. M., Campillo, M., Stehly, L., & Ritzwoller, M. H. (2005). High-resolution surface-wave tomography from ambient seismic noise. *Science*, *307*(5715), 1615–1618. <https://doi.org/10.1126/science.1108339>
- Shepherd, A., Ivins, E. R., Geruo, A., Barletta, V. R., Bentley, M. J., Bettadpur, S., et al. (2012). A reconciled estimate of ice-sheet mass balance. *Science*, *338*(6111), 1183–1189. <https://doi.org/10.1126/science.1228102>
- Sladen, A., Rivet, D., Ampuero, J. P., De Barros, L., Hello, Y., Calbris, G., & Lamare, P. (2019). Distributed sensing of earthquakes and ocean-solid Earth interactions on seafloor telecom cables. *Nature Communications*, *10*(1), 5777. <https://doi.org/10.1038/s41467-019-13793-z>
- Slichter, L. B. (1932). The theory of the interpretation of seismic travel-time curves in horizontal structures. *Physics*, *3*(6), 273–295. <https://doi.org/10.1063/1.1745133>
- Smith, A. M. (1997). Variations in basal conditions on Rutford Ice Stream, West Antarctica. *Journal of Glaciology*, *43*(144), 245–255. <https://doi.org/10.3189/S0022143000003191>
- Smith, A. M., Anker, P. G. D., Nicholls, K. W., Makinson, K., Murray, T., Rios-Costas, S., et al. (2021). Ice stream subglacial access for ice-sheet history and fast ice flow: The BEAMISH project on Rutford Ice Stream, West Antarctica and initial results on basal conditions. *Annals of Glaciology*, *62*(85–86), 203–211. <https://doi.org/10.1017/aog.2020.82>
- Smith, E. C., Baird, A. F., Kendall, J. M., Martin, C., White, R. S., Brisbourne, A. M., & Smith, A. M. (2017). Ice fabric in an Antarctic ice stream interpreted from seismic anisotropy. *Geophysical Research Letters*, *44*(8), 3710–3718. <https://doi.org/10.1002/2016GL072093>
- Smith, E. C., Smith, A. M., White, R. S., Brisbourne, A. M., & Pritchard, H. D. (2015). Mapping the ice-bed interface characteristics of Rutford Ice Stream, West Antarctica, using microseismicity. *Journal of Geophysical Research: Earth Surface*, *120*(9), 1881–1894. <https://doi.org/10.1002/2015JF003587>
- Snieder, R. (2004). Extracting the Green's function from the correlation of coda waves: A derivation based on stationary phase. *Physical Review E*, *69*(4), 046610. <https://doi.org/10.1103/physreve.69.046610>
- Snieder, R., & Larose, E. (2013). Extracting Earth's elastic wave response from noise measurements. *Annual Review of Earth and Planetary Sciences*, *41*(1), 183–206. <https://doi.org/10.1146/annurev-earth-050212-123936>
- Spica, Z. J., Nishida, K., Akuhara, T., Pétréris, F., Shinohara, M., & Yamada, T. (2020). Marine Sediment characterized by ocean-bottom fiber-optic seismology. *Geophysical Research Letters*, *47*(16), e2020GL088360. <https://doi.org/10.1029/2020GL088360>
- Spica, Z. J., Perton, M., Martin, E. R., Beroza, G. C., & Biondi, B. (2020). Urban seismic site characterization by fiber-optic seismology. *Journal of Geophysical Research: Solid Earth*, *125*(3), 1–14. <https://doi.org/10.1029/2019JB018656>
- Tribaldos, V. R., Ajo-Franklin, J. B., Dou, S., Lindsey, N. J., Ulrich, C., Robertson, M., et al. (2021). Surface wave imaging using distributed acoustic sensing deployed on dark fiber. Distributed acoustic sensing in geophysics (pp. 197–212). <https://doi.org/10.1002/9781119521808.ch15>

- van den Broeke, M. (2005). Strong surface melting preceded collapse of Antarctic Peninsula Ice shelf. *Geophysical Research Letters*, 32(12), 1–4. <https://doi.org/10.1029/2005GL023247>
- van den Broeke, M. (2008). Depth and density of the Antarctic firn layer. *Arctic Antarctic and Alpine Research*, 40(2), 432–438. [https://doi.org/10.1657/1523-0430\(07-021](https://doi.org/10.1657/1523-0430(07-021)
- van den Ende, M. P. A., & Ampuero, J. P. (2021). Evaluating seismic beamforming capabilities of distributed acoustic sensing arrays. *Solid Earth*, 12(4), 915–934. <https://doi.org/10.5194/se-12-915-2021>
- Vidal, C. A., Draganov, D., van der Neut, J., Drijkoningen, G., & Wapenaar, K. (2014). Retrieval of reflections from ambient noise using illumination diagnosis. *Geophysical Journal International*, 198(3), 1572–1584. <https://doi.org/10.1093/gji/ggu164>
- Walter, F., Gräff, D., Lindner, F., Paitz, P., Köpfl, M., Chmiel, M., & Fichtner, A. (2020). Distributed acoustic sensing of microseismic sources and wave propagation in glaciated terrain. *Nature Communications*, 11(1), 2436. <https://doi.org/10.1038/s41467-020-15824-6>
- Walter, F., Roux, P., Roeoesli, C., Lecointre, A., Kilb, D., & Roux, P. F. (2015). Using glacier seismicity for phase velocity measurements and Green's function retrieval. *Geophysical Journal International*, 201(3), 1722–1737. <https://doi.org/10.1093/gji/ggv069>
- Williams, A. (2022). *Fibre optic cables as distributed acoustic sensors: Applications in seismology [PhD thesis]*. University of Bristol.
- Williams, E. F., Fernández-Ruiz, M. R., Magalhaes, R., Vanthillo, R., Zhan, Z., González-Herráez, M., & Martins, H. F. (2019). Distributed sensing of microseisms and teleseisms with submarine dark fibers. *Nature Communications*, 10(1), 1–11. <https://doi.org/10.1038/s41467-019-13262-7>
- Xia, J., Miller, R. D., & Park, C. B. (1999). Estimation of near-surface shear-wave velocity by inversion of Rayleigh waves. *Geophysics*, 64(3), 691–700. <https://doi.org/10.1190/1.1444578>
- Xia, J., Xu, Y., & Miller, R. D. (2007). Generating an image of dispersive energy by frequency decomposition and slant stacking. *Pure and Applied Geophysics*, 164(5), 941–956. <https://doi.org/10.1007/s00024-007-0204-9>
- Yu, C., Zhan, Z., Lindsey, N. J., Ajo-Franklin, J. B., & Robertson, M. (2019). The potential of DAS in teleseismic studies: Insights from the Goldstone experiment. *Geophysical Research Letters*, 46(3), 1320–1328. <https://doi.org/10.1029/2018GL081195>
- Yudistira, T., Paulssen, H., & Trampert, J. (2017). The crustal structure beneath The Netherlands derived from ambient seismic noise. *Tectonophysics*, 721, 361–371. <https://doi.org/10.1016/j.tecto.2017.09.025>
- Zhang, X., Paulssen, H., Lebedev, S., & Meier, T. (2007). Surface wave tomography of the Gulf of California. *Geophysical Research Letters*, 34(15). <https://doi.org/10.1029/2007GL030631>
- Zhou, W., & Paulssen, H. (2020). Compaction of the Groningen gas reservoir investigated with train noise. *Geophysical Journal International*, 223(2), 1327–1337. <https://doi.org/10.1093/gji/ggaa364>
- Zhou, W., Butcher, A., Brisbourne, A., Kufner, S., Kendall, J. M., & Stork, A. (2022). Seismic noise interferometry and distributed acoustic sensing (DAS): Inverting for the firn layer S-velocity structure on Rutford Ice Stream, Antarctica (v.0.0.1) [Dataset]. Zenodo. <https://doi.org/10.5281/zenodo.7064405>